Near-Threshold Inelastic Collisions Using Molecular Beams with a Tunable Velocity

Joop J. Gilijamse,[1] Steven Hoekstra,[1] Sebastiaan Y. T. van de Meerakker,[1]*
Gerrit C. Groenenboom,[2]* Gerard Meijer[1]

Molecular scattering behavior has generally proven difficult to study at low collision energies. We formed a molecular beam of OH radicals with a narrow velocity distribution and a tunable absolute velocity by passing the beam through a Stark decelerator. The transition probabilities for inelastic scattering of the OH radicals with Xe atoms were measured as a function of the collision energy in the range of 50 to 400 wavenumbers, with an overall energy resolution of about 13 wavenumbers. The behavior of the cross-sections for inelastic scattering near the energetic thresholds was accurately measured, and excellent agreement was obtained with cross-sections derived from coupled-channel calculations on ab initio computed potential energy surfaces.

The study of collisions between gas-phase atoms and molecules is a well-established method of gathering detailed information about their individual structures and mutual interaction (*1*). The level of detail obtained by these studies depends on the quality of preparation of the collision partners before the collision (*2*–*4*) and on how accurately the products are analyzed afterward (*5*–*7*). In recent years, it has become increasingly possible to control the internal and external degrees of freedom of the scattering partners, allowing the potential energy surfaces that govern the molecular collisions to be probed in ever greater detail. The most detailed information is obtained when crossed molecular beams are used to produce intense jets of molecules with a well-defined velocity, confined to only a few internal quantum states. Further state selection can be achieved by optical preparation of a single quantum state or by purification of the beam with the use of electrostatic or magnetic multipole fields (*2*, *3*). These methods allow the orientation of the molecules to be controlled before the collision (*8*, *9*) and the orientation of the scattered products to be measured (*10*).

One of the most important parameters describing a scattering event is the collision energy of the scatterers. However, control over the collision energy has been a difficult experimental task. Since the 1980s, ingenious crossed-beam machines have been engineered to vary the crossing angle of the intersecting beams, allowing variation of the collision energy while maintaining particle densities high enough for scattering (*11*). It was thereby possible to measure threshold behavior of rotational energy transfer (*12*, *13*) or to tune the collision energy over the reaction barrier for reactive scattering (*14*, *15*). These methods led to considerable improvement in the control over collision energy at high energies—for example, to probe short-range interactions. However, a similar level of control over collisions at low energies, which are sensitive probes for long-range interactions, is generally lacking. The angle of the intersecting beams cannot be varied to arbitrarily small values; and at low collision energies, the energy resolution, which is determined by the velocity spread of both beams, rapidly becomes comparable to the collision energy.

Low-energy collisions of atoms and molecules interrogate the part of the interaction potential energy surface that is relevant for the formation of long-lived complexes. From resonance phenomena in the scattering signal as a function of collision energy, accurate information on the interaction can be extracted (*16*–*18*). Near the energetic thresholds for inelastic scattering, resonant states can be formed when the colliding complex begins to rotate, leaving the constituents with insufficient translational energy to overcome their van der Waals attraction. Methods to experimentally extract information on these resonances are extremely limited. Thus far, low-energy collisions have only been studied in cryogenic cell environments (*19*) or in supersonic gas expansions that are specifically designed to maintain a thermal equilibrium at temperatures as low as 6 K (*20*). Recently, reports have appeared on the study of cold inelastic collisions between alkali atoms and dimers in an optically trapped gas (*21*, *22*).

An alternative experimental approach to studying collisions at a low and/or variable energy is to produce molecular beams with a low and/or variable velocity (*23*). Mechanical velocity selectors can be used to select molecules with a narrow velocity distribution out of molecular beams (*24*), but the particle densities and velocities that can be reached are set by the original velocity distribution of the beam. Exquisite control over the velocity of polar molecules in a molecular beam has only been possible since the development of the Stark deceleration technique. The Stark decelerator for neutral polar molecules is the equivalent of a linear accelerator for charged particles and exploits the interaction of a polar molecule with inhomogeneous time-varying electric fields (*25*, *26*). The deceleration (or acceleration) process can be seen as slicing a packet of molecules with a narrow velocity distribution out of the densest part of the molecular beam pulse. This packet can then be decelerated or accelerated to any velocity, maintaining the narrow velocity distribution and the particle density in the packet. In a crossed-beam configuration, this tool offers the revolutionary capability to study elastic or inelastic and reactive scattering as a function of the continuously variable collision energy, from low to high collision energies, and with a high intrinsic energy resolution. The computer-controlled velocity of the molecular beam allows scanning of the collision energy in an otherwise fixed experimental geometry. The deceleration process is highly quantum-state specific, and the state purity of the bunches of selected molecules that emerge from the decelerator can be close to 100%. Moreover, the decelerated molecules are all naturally spatially oriented, and steric effects can therefore in principle be studied as well.

Here, we report the use of a Stark-decelerated molecular beam with a tunable and narrow velocity distribution in a molecular beam scattering experiment. In a crossed-beam setup, rotationally inelastic scattering between state-selected OH radicals [$X^2\Pi_{3/2}$, $v = 0$, $J = 3/2$, f (*27*), referred to hereafter as $F_1(3/2f)$] and Xe atoms is studied throughout the 0.14 to 1.14 kcal/mol (50 to 400 cm^{-1}) region, with an overall energy resolution of ~0.03 kcal/mol (13 cm^{-1}). We chose the OH–rare gas system because at higher collision energies, rotationally inelastic collisions have been studied for this system in great detail, both experimentally and theoretically; state-to-state cross-sections and the effects of molecular orientation have been determined (*28*, *29*). The energy range covered in this study encompassed the energetic thresholds for inelastic scattering down to the lowest rotational levels of OH. The threshold behavior of the inelastic state-to-state cross-sections was accurately measured and was compared with the outcome of coupled-channels calculations on a computed OH-Xe potential energy surface.

A molecular beam of OH radicals in the low-field–seeking $F_1(3/2f)$ state was decelerated, guided, or accelerated with the use of a Stark decelerator (Fig. 1). The time-of-flight profile of the radicals that exit the decelerator is shown for a typical setting of the decelerator. The densest part of the OH beam, with an original velocity of 450 m/s, was selected and slowed down to a final velocity of 281 m/s. The

[1]Fritz-Haber-Institut der Max-Planck-Gesellschaft, Faradayweg 4-6, 14195 Berlin, Germany. [2]Theoretical Chemistry, Institute for Molecules and Materials, Radboud University Nijmegen, Toernooiveld 1, 6525 ED Nijmegen, Netherlands.

*To whom correspondence should be addressed. E-mail: basvdm@fhi-berlin.mpg.de (S.Y.T.M.); gerritg@theochem.ru.nl (G.C.G.)

decelerated packet of radicals arrived temporally delayed in the field-free interaction region and was scattered with a beam of pure Xe under an angle of 90°. In the experiments, the velocity of the OH radicals was varied from 33 to 700 m/s; the contribution of the OH radicals to the center-of-mass (CM) collision energy (E_{coll}) was thereby varied from less than 1 to ~310 cm^{-1}. The contribution of the width of the OH velocity distribution to the overall energy resolution was very small. The maximum rotational state purity of the packet of OH $F_1(3/2f)$ radicals before the collision was measured to be ≥99.7%. Contamination of the inelastic state-to-state scattering data by initial populations in different quantum states was negligible.

The xenon beam was produced by expansion of Xe at 2.5-atm backing pressure from a cooled pulsed valve (−70°C), resulting in a beam with a velocity of ~300 m/s. The exact velocity of the Xe atoms depends on the detailed settings of the pulsed valve as well as the timing of the collision event within the Xe gas pulse, and these settings were kept fixed during the measurements. Although the exact velocity of the Xe atoms was not measured, the constant contribution of the Xe atoms to the CM collision energy of ~60 cm^{-1} was sufficiently low that the total CM collision energy could be tuned over the energetic thresholds for scattering into both parity components of the $F_1(5/2)$ level (84 cm^{-1} excitation energy) and the $F_2(1/2)$ level (121 cm^{-1} excitation energy). The approximate 10% velocity spread in the Xe beam was by far the dominant contribution to the overall energy resolution in this experiment.

Saturated laser-induced fluorescence with tunable pulsed lasers was used to detect the OH radicals (*30*). For each setting of the OH velocity, the populations in the $F_1(3/2e)$, $F_1(3/2f)$, $F_1(5/2e)$, $F_1(5/2f)$, and $F_2(1/2e)$ levels were measured, both with and without collision of the Xe beam with the OH beam. The decrease of population in the $F_1(3/2f)$ level due to scattering with the Xe atoms was about 1%, indicating that single-collision conditions were fulfilled in the experiment. The signals associated with the scattering products were normalized by the signal of the incoming OH $F_1(3/2f)$ radical beam. Different excitation rates for the different branches of the optical transitions used to probe the different levels were taken into account to relate signal intensities to populations. Thus, transition probabilities for inelastic scattering to the $F_1(3/2e)$, $F_1(5/2e)$, $F_1(5/2f)$, and $F_2(1/2e)$ levels were obtained as a function of the OH contribution to the CM collision energy (Fig. 2). Collisions populating the $F_1(3/2e)$ level were most likely. Within the $F_1(5/2)$ level, collisions populating the lower Λ-doublet component of *e* parity were favored, consistent with findings of other $^2\Pi$–rare gas systems (*28*, *29*). For the $F_1(3/2e)$ and the $F_1(5/2e)$ and $F_1(5/2f)$ levels, the transition probabilities were almost constant at higher collision energies. Close to the $F_1(5/2)$ energetic threshold, collisions populating either one of the parity components of this level became less probable, and the transition probabilities for these levels dropped sharply. The only inelastic channel that was exoenergetic was scattering to the $F_1(3/2e)$ level, and its transition probability showed an increase at low collision energies. Excitation to the $F_2(1/2)$ level required a spin-orbit–changing collision, for which the cross-sections are generally lower than for a spin-orbit–conserving collision. The transition probability for this channel also showed a clear threshold behavior.

The theoretical framework to compute cross-sections for inelastic collisions of $^2\Pi$-state molecules such as OH with ^1S-state atoms such as Xe is well established (*31*). The electronic degeneracy of the Π state is lifted upon the approach of the atom, and two potential energy surfaces are required to describe the system. Contour plots of the potentials are shown in Fig. 3. We computed the potentials with the partially spin-restricted open-shell coupled-

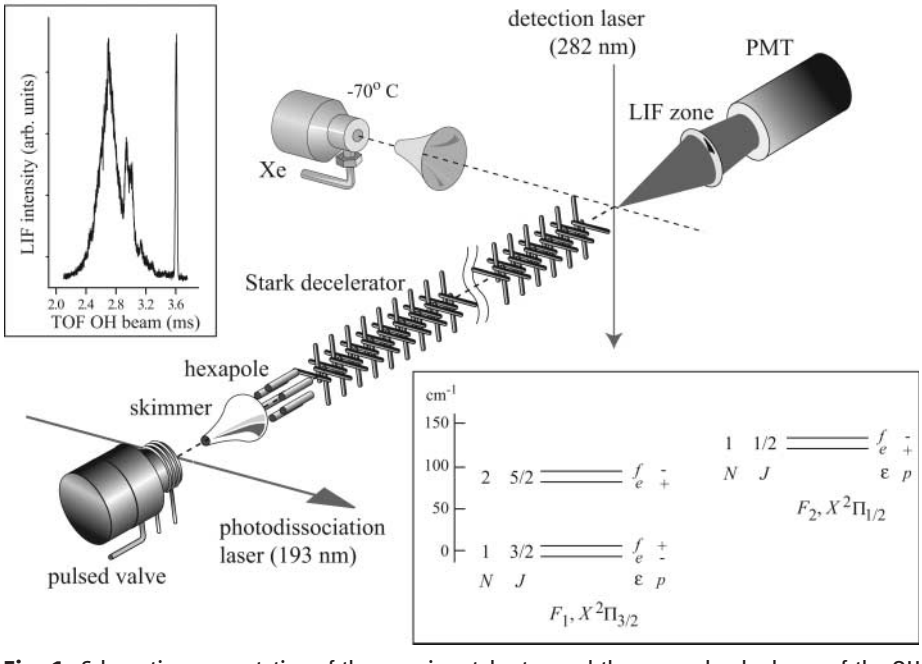

Fig. 1. Schematic representation of the experimental setup and the energy-level scheme of the OH radical. The OH radical beam is produced by photodissociation of gaseous HNO_3 that is coexpanded with a noble carrier gas (Ar, Kr, or Xe) into a vacuum. The beam is skimmed and radicals in the low-field–seeking $F_1(3/2f)$ state are focused with a hexapole into the Stark decelerator, where the beam is decelerated, guided, or accelerated to a velocity in the 33 to 700 m/s range. A typical time-of-flight (TOF) profile is shown in the left inset. The selected packet of radicals arrives temporally separated in the scattering region and is scattered with a beam of pure Xe at an angle of 90°, under single-collision conditions. The collision-induced populations in the $F_2(1/2)$, $F_1(3/2)$, and $F_1(5/2)$ rotational levels are probed before and after the collisions using a pulsed dye laser system in a saturated laser-induced fluorescence (LIF) scheme. The fluorescence is imaged onto a photomultiplier tube (PMT). In the energy-level scheme shown in the right inset, the splitting between both parity components of each rotational level is largely exaggerated for reasons of clarity.

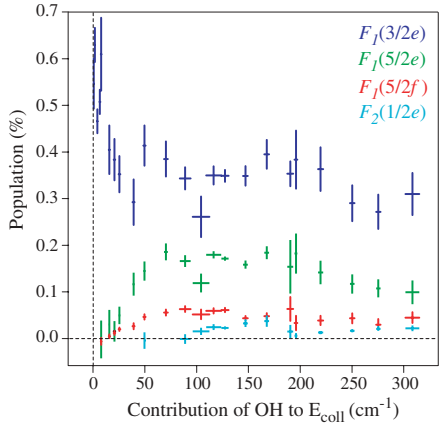

Fig. 2. Probabilities for inelastic scattering of OH $F_1(3/2f)$ radicals in collisions with Xe atoms to the $F_1(3/2e)$, $F_1(5/2e)$, $F_1(5/2f)$, and the $F_2(1/2e)$ levels as a function of [1/2] $[(m_{OH}m_{Xe})/(m_{OH} + m_{Xe})]$ v_{OH}^2—i.e., as a function of the contribution of OH to the CM collision energy (where m_{OH} and m_{Xe} are the mass of OH and Xe, respectively, and v_{OH} is the velocity of the OH radicals in the laboratory frame). The horizontal error bars represent the uncertainty in collision energy that results from the velocity spread of the OH beam, which is different for every setting of the decelerator. The vertical error bars represent the statistical spread of the data as obtained from repeated runs of the experiment.

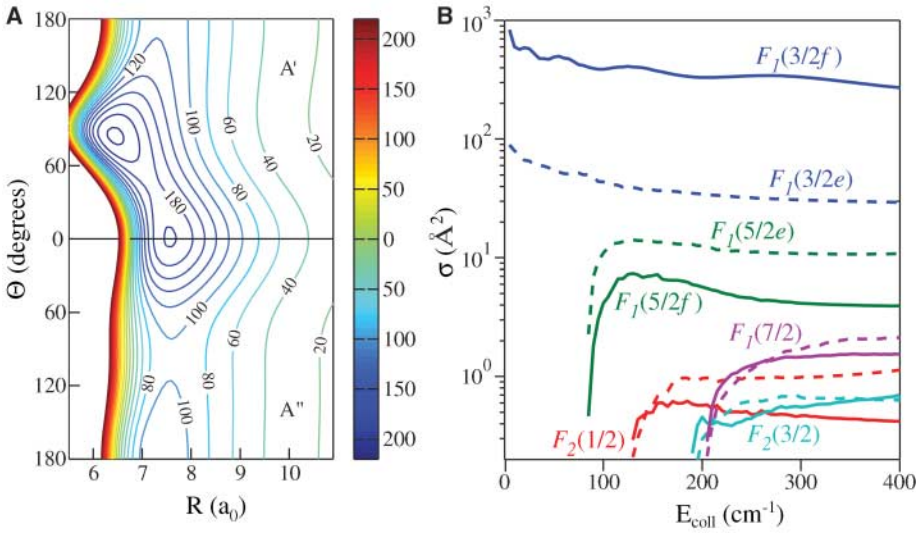

Fig. 3. (**A**) Contour plots of the A' (upper) and A'' (lower) potential surfaces in cm^{-1}. The potentials are computed with the RCCSD(T) method. A large one-electron basis consisting of the augmented-correlation consistent polarized valence quadruple zeta (aug-cc-pVQZ) set is used, extended with a set of (*3s*, *3p*, *2d*, *1f*, and *1g*) mid-bond orbitals with geometry-dependent exponents (*38*). The angular dependence of the sum of the potentials is represented by a Legendre polynomial expansion and the difference of the two potentials by associated Legendre functions, as required by theory (*31*). The proper R^{-n} analytic form is used for the radial dependence of the long-range expansion of the sum potential, and the reproducing kernel Hilbert space interpolation method (*39*) is used for the radial dependence of the short and intermediate range of the sum potential and for the difference potential. We tested the fit by performing additional ab initio calculations for 75 random geometries and found it to be very accurate: The errors at these points were on the order of a few tenths of a cm^{-1} or less. A fortran code of the potentials is available as supporting online material. (**B**) Computed cross sections for the first 10 channels, computed on a collision energy grid of E_{coll} = 5, 10, 15, …, 400 cm^{-1}. The solid and dashed lines correspond to channels of *f* and *e* spectroscopic labeling, respectively. The $F_1(3/2f)$ channel is the elastic channel. In the Hamiltonian we used the OH rotational constant B = 18.5487 cm^{-1}, the spin-orbit coupling constant A = −139.21 cm^{-1}, and Λ-doubling parameters p = 0.235 cm^{-1} and q = −0.0391 cm^{-1}. The channel basis included all OH rotational states with angular momentum $J \leq 21/2$. The highest total angular momentum in the basis has $F = 271/2$ and all $F \leq 201/2$ are present. The renormalized Numerov method was used to propagate the wave function from R = 4 to 35 a_0, where a_0 is the Bohr radius. Our computer code is verified by reproducing bound-state and scattering calculations on similar systems from the literature.

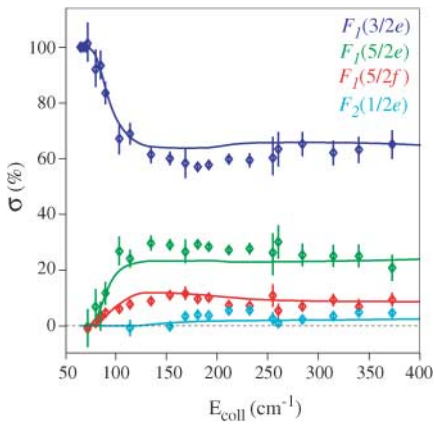

Fig. 4. Comparison of the collision energy dependence of the measured (data points with error bars) and calculated (solid curves) relative cross-sections—i.e., the fractional scattering of OH radicals into one of the $F_1(3/2e)$, $F_1(5/2e)$, $F_1(5/2f)$, or $F_2(1/2e)$ channels.

cluster method with single and double excitations and perturbative triples [RCCSD(T)] (*32*), as implemented in the MOLPRO 2002 program package (*33*). Interaction energies were obtained as the difference between the energy of the complex and the energies of the fragments. We computed the fragments in the same one-electron basis set as the complex to avoid the so-called basis set superposition error. This method is one of the best available to compute highly accurate potentials of weakly interacting systems. The Xe atom has 54 electrons; the 28 inner shell electrons are described by a relativistic pseudopotential (*34*). The interaction energies were computed for 300 geometries on a two-dimensional grid with 15 Gauss-Legendre points in the Jacobi-angle (θ) and atom-molecule separations up to R = 20 a_0. The OH bond length is kept fixed at r_0 = 1.8502 a_0. We used an analytical representation of the potentials (Fig. 3). The global minimum of −224 cm^{-1} occurs on the A' potential for a T-shaped geometry. This potential has a local minimum for a linear OH-Xe geometry (θ = 0°).

To compute the inelastic cross-sections, we performed fully converged coupled-channel calculations. The Hamiltonian includes the OH rotational, spin-orbit, and Λ-doubling terms. We used the *R*-embedded body-fixed channel basis for which the potential energy matrix elements are given in (*35*). Convergence of the cross-sections with respect to all parameters has been tested to be better than 1%. According to Wigner's threshold laws (*36*), the inelastic cross-sections at low energies are proportional to the square root of the excess energy. We found that in this case, a square root energy dependence holds approximately for several points above threshold on our 5 cm^{-1} interval grid as well.

Relating the measured energy-dependent transition probabilities (Fig. 2) to the calculated inelastic cross-sections (Fig. 3) requires detailed information on the relative velocity of the scatterers, the actual time interval during which scattering events are probed, and the detection probability of the scattered products (*12*). Systematic effects, such as the collision energy–dependent time interval for scattering and intensity and velocity of the incoming OH beam, cancel out when the relative inelastic transition probabilities are extracted from the measured absolute transition probabilities given in Fig. 2. If we assume an identical detection probability of the scattered products for the different inelastic channels for a given collision energy (*37*), the relative inelastic transition probabilities directly yield the relative cross-sections for inelastic scattering (Fig. 4). The horizontal axis is given an offset compared with the one in Fig. 2 to include the contribution of the Xe atoms to E_{coll}. The positions of the energetic thresholds are known with spectroscopic accuracy, and we obtained the best agreement when a velocity of the Xe atoms of 320 m/s was taken. The theoretical inelastic cross-sections (Fig. 3) were first convoluted with the experimental energy resolution, and we used the resultant values to calculate the relative cross-sections (solid curves in Fig. 4). Excellent agreement between theory and experiment was obtained throughout the range of collision energies probed. The ratio of scattering into the different channels, and, in particular, the shape of the inelastic cross-sections around threshold is perfectly reproduced.

Our measurements provide a very sensitive probe for the theoretical potential energy surfaces, from which a detailed understanding of the collision dynamics can be obtained. A next step will be to use two crossed velocity-tunable molecular beams or to collide the velocity-tunable beam with a stationary (i.e., trapped) sample of cold or ultracold atoms or molecules. In such systems, quantum state–selected atom-molecule and molecule-molecule collisions can be studied, down to collision energies less than 1 cm^{-1}, with a fraction of a wavenumber energy resolution.

References and Notes

1. R. D. Levine, R. B. Bernstein, *Molecular Reaction Dynamics and Chemical Reactivity,* (Oxford Univ. Press, New York, 1987).

2. G. Scoles, Ed., *Atomic and Molecular Beam Methods* (Oxford Univ. Press, New York, 1988), vol. 1.
3. G. Scoles, Ed., *Atomic and Molecular Beam Methods* (Oxford Univ. Press, New York, 1992), vol. 2.
4. T. P. Rakitzis, A. J. van den Brom, M. H. M. Janssen, *Science* **303**, 1852 (2004).
5. X. Liu, J. J. Lin, S. Harich, G. C. Schatz, X. Yang, *Science* **289**, 1536 (2000).
6. S. A. Harich *et al.*, *Nature* **419**, 281 (2002).
7. J. J. Lin, J. Zhou, W. Shiu, K. Liu, *Science* **300**, 966 (2003).
8. J. J. van Leuken, J. Bulthuis, S. Stolte, J. G. Snijders, *Chem. Phys. Lett.* **260**, 595 (1996).
9. R. N. Zare, *Science* **279**, 1875 (1998).
10. M. C. van Beek, G. Berden, H. L. Bethlem, J. J. ter Meulen, *Phys. Rev. Lett.* **86**, 4001 (2001).
11. G. Hall, K. Liu, M. J. McAuliffe, C. F. Giese, W. R. Gentry, *J. Chem. Phys.* **78**, 5260 (1983).
12. R. G. Macdonald, K. Liu, *J. Chem. Phys.* **91**, 821 (1989).
13. D. M. Sonnenfroh, R. G. Macdonald, K. Liu, *J. Chem. Phys.* **94**, 6508 (1991).
14. R. T. Skodje *et al.*, *Phys. Rev. Lett.* **85**, 1206 (2000).
15. D. Skouteris *et al.*, *Science* **286**, 1713 (1999).
16. W. Shiu, J. J. Lin, K. Liu, *Phys. Rev. Lett.* **92**, 103201 (2004).
17. R. C. Forrey, N. Balakrishnan, V. Kharchenko, A. Dalgarno, *Phys. Rev. A.* **58**, R2645 (1998).
18. N. Balakrishnan, A. Dalgarno, R. C. Forrey, *J. Chem. Phys.* **113**, 621 (2000).
19. C. D. Ball, F. C. De Lucia, *Phys. Rev. Lett.* **81**, 305 (1998).
20. I. R. Sims *et al.*, *J. Chem. Phys.* **97**, 8798 (1992).
21. P. Staanum, S. D. Kraft, J. Lange, R. Wester, M. Weidemüller, *Phys. Rev. Lett.* **96**, 023201 (2006).
22. N. Zahzam, T. Vogt, M. Mudrich, D. Comparat, P. Pillet, *Phys. Rev. Lett.* **96**, 023202 (2006).
23. C. E. Heiner, H. L. Bethlem, G. Meijer, *Phys. Chem. Chem. Phys.* **8**, 2666 (2006) and references therein.
24. L. T. Cowley, M. A. D. Fluendy, K. P. Lawley, *Rev. Sci. Instrum.* **41**, 666 (1970).
25. H. L. Bethlem, G. Berden, G. Meijer, *Phys. Rev. Lett.* **83**, 1558 (1999).
26. H. L. Bethlem, G. Meijer, *Int. Rev. Phys. Chem.* **22**, 73 (2003).
27. The labels $X^2\Pi_{3/2}$, v, and J indicate the electronic, vibrational, and rotational state of the OH radical, respectively. The spectroscopic symmetry labels *e* and *f* refer to the total parity of the electronic wavefunction, exclusive of rotation.
28. M. C. van Beek, J. J. ter Meulen, M. H. Alexander, *J. Chem. Phys.* **113**, 628 (2000).
29. M. C. van Beek, J. J. ter Meulen, M. H. Alexander, *J. Chem. Phys.* **113**, 637 (2000).
30. S. Y. T. van de Meerakker, N. Vanhaecke, G. Meijer, *Annu. Rev. Phys. Chem.* **57**, 159 (2006).
31. M. H. Alexander, *J. Chem. Phys.* **76**, 5974 (1982).
32. P. J. Knowles, C. Hampel, H.-J. Werner, *J. Chem. Phys.* **99**, 5219 (1993).
33. MOLPRO, version 2002.6, a package of ab initio programs, H. J. Werner, P. J. Knowles, R. Lindh, F. R. Manby, M. Schütz, and others, Cardiff, UK (www.molpro.net).
34. K. A. Peterson, D. Figgen, E. Goll, H. Stoll, M. Dolg, *J. Chem. Phys.* **119**, 11113 (2003).
35. G. Dhont, W. B. Zeimen, G. C. Groenenboom, A. van der Avoird, *J. Chem. Phys.* **120**, 103 (2004).
36. E. P. Wigner, *Phys. Rev.* **73**, 1002 (1948).
37. The validity of this assumption is verified by analytically modeling the detection probability in the limiting cases of forward, backward, and isotropic scattering. The difference is found to be within the error bars of our data.
38. G. C. Groenenboom, N. Balakrishnan, *J. Chem. Phys.* **118**, 7380 (2003).
39. T.-S. Ho, H. Rabitz, *J. Chem. Phys.* **104**, 2584 (1996).

40. This research is supported by the European Union Cold Molecules Network. We thank N. Vanhaecke for help preparing this experiment and D. W. Chandler for many fruitful discussions and for carefully reading the manuscript.

Supporting Online Material

www.sciencemag.org/cgi/content/full/313/5793/1617/DC1
Computer Codes

28 June 2006; accepted 7 August 2006
10.1126/science.1131867

Evidence for a Polar Ethane Cloud on Titan

C. A. Griffith,[1]* P. Penteado,[1] P. Rannou,[2] R. Brown,[1] V. Boudon,[3] K. H. Baines,[4] R. Clark,[5] P. Drossart,[6] B. Buratti,[4] P. Nicholson,[7] C. P. McKay,[8] A. Coustenis,[6] A. Negrao,[2,9] R. Jaumann[10]

Spectra from Cassini's Visual and Infrared Mapping Spectrometer reveal the presence of a vast tropospheric cloud on Titan at latitudes 51° to 68° north and all longitudes observed (10° to 190° west). The derived characteristics indicate that this cloud is composed of ethane and forms as a result of stratospheric subsidence and the particularly cool conditions near the moon's north pole. Preferential condensation of ethane, perhaps as ice, at Titan's poles during the winters may partially explain the lack of liquid ethane oceans on Titan's surface at middle and lower latitudes.

Past images of Saturn's largest moon, Titan, display large clouds only where solar heating is greatest, which presently occurs at high southern latitudes (*1*–*3*). The morphology of Titan's southern clouds indicates that they are convective, composed of methane, and result from the summer heating of Titan's surface and updrafts from Titan's summer Hadley cell (*1*, *4*–*6*). Similar processes instigate the formation of thunderstorms on Earth. The latent heat of Titan's major condensable constituent, methane, is large enough that, like water on Earth, adiabatic lifting and consequent cooling of air cause cloud formation (*7*). In contrast, at high northern latitudes, air circulates downward from the dry stratosphere (above an altitude of 40 km) and is heated through compression, which prevents the formation of methane clouds.

Spectral images of Titan's northern hemisphere, recorded by Cassini's Visual and Infrared Mapping Spectrometer (VIMS) (*8*), indicate a ubiquitous bright band at 51° to 68°N latitude, at the edge of Titan's arctic circle (Fig. 1). Its presence at higher latitudes cannot be determined because of a lack of illumination. The band appears at wavelengths that detect altitudes above 30 km (1.9, 2.13, and 2.7 to 2.9 μm) yet not at wavelengths that probe altitudes above 60 km (for example, at 1.67, 2.25, and 3.2 μm), indicating that particles near an altitude of 40 km are the cause (Fig. 2). Unlike Titan's southern clouds, this northern cloud shows no hourly variability and is diffusely spread over a large area, with only small continuous variations in optical depth between adjacent pixels (Fig. 1).

The cloud appears at latitudes where Titan's general circulation concentrates and transports photochemical products, principally ethane, to lower altitudes, where they condense and may form clouds (*6*). Methane (the second most abundant atmospheric constituent after nitrogen) is dissociated irreversibly by solar ultraviolet light, producing primarily ethane and, at one-sixth and one-10th of the ethane production rate, respectively, acetylene and haze, as well as other less abundant organic molecules (*9*, *10*). These photochemical by-products precipitate to Titan's surface. Titan's atmospheric composition and photochemical models indicate that ethane accumulates as a liquid (at the equatorial surface temperature of 93.5 K) at a rate of ~300 m (if global) over Titan's lifetime of 4.5 billion years, whereas solid sediments, including acetylene and haze particles, accumulate at roughly one-third of this rate (*10*). Thus, unless methane is a recent addition to Titan's atmosphere (*11*) or ethane incorporates itself into surface solids (*12*), it has been reasoned that a considerable fraction of the surface should be covered with liquid ethane (*13*). Titan's surface reveals dunes of solid sediments, probably including haze particles and acetylene ice (*14*). In addition, the surface is riddled with alluvial features (*15*–*17*), suggesting the occurrence of methane rain in the past. Craters are rare, indicating geological relaxation as well as their burial by photochemical sediments (*15*, *16*, *18*). Yet Titan appears depleted of its most abundant photochemical by-product. Except for the ethane-damp surface measured by Huygens (*19*), no condensed form of ethane has been detected (*20*), despite its rapid production in Titan's stratosphere and

[1]Lunar and Planetary Laboratory, University of Arizona, Tucson, AZ, 85721 USA. [2]Service d'Aéronomie, Université de Versailles-St-Quentin, BP3, 91371 Verriéres le Buisson, France. [3]Laboratoire de Physique de l'Université de Bourgogne, CNRS UMR 5027, Boîte Postale 47870, F-21078 Dijon, France. [4]Jet Propulsion Laboratory, California Institute of Technology, Pasadena, CA, 91109 USA. [5]U.S. Geological Survey, Denver, CO, 80225 USA. [6]Observatoire de Paris, 5 Place Jules Jannsen, Meudon, France. [7]Department of Astronomy, Cornell University, Ithaca, NY, USA. [8]National Aeronautics and Space Administration, Ames Research Center, Moffett Field, Mountain View, CA, USA. [9]Observatório Astronómico de Lisboa, 1349–018 Lisboa, Portugal. [10]Institute of Planetary Exploration, Deutsche Zentrum für Luft- und Raumfahrt, Germany.